



**HAL**  
open science

# Surface topographic impact of subglacial water beneath Mars' south polar ice cap

N. Arnold, F. Butcher, S. Conway, C. Gallagher, M. Balme

► **To cite this version:**

N. Arnold, F. Butcher, S. Conway, C. Gallagher, M. Balme. Surface topographic impact of subglacial water beneath Mars' south polar ice cap. *Nature Astronomy*, In press, 10.1038/s41550-022-01782-0 . insu-03813438

**HAL Id: insu-03813438**

**<https://insu.hal.science/insu-03813438>**

Submitted on 13 Oct 2022

**HAL** is a multi-disciplinary open access archive for the deposit and dissemination of scientific research documents, whether they are published or not. The documents may come from teaching and research institutions in France or abroad, or from public or private research centers.

L'archive ouverte pluridisciplinaire **HAL**, est destinée au dépôt et à la diffusion de documents scientifiques de niveau recherche, publiés ou non, émanant des établissements d'enseignement et de recherche français ou étrangers, des laboratoires publics ou privés.

1 Surface topographic impact of subglacial water beneath Mars'  
2 south polar ice cap

3 N.S. Arnold<sup>1\*</sup>, F.E.G. Butcher<sup>2\*</sup>, S.J. Conway<sup>3</sup>, C. Gallagher<sup>4</sup> and M.R.  
4 Balme<sup>5</sup>

5 1. Scott Polar Research Institute, University of Cambridge, Lensfield  
6 Road, Cambridge, CB2 1ER, UK.

7 2. Department of Geography, The University of Sheffield, Winter Street,  
8 Sheffield, S10 2TN, UK

9 3. CNRS, UMR 6112 Laboratoire de Planétologie et Géodynamique,  
10 Université de Nantes, France

11 4. UCD School of Geography, Newman Building, University College Dublin,  
12 Belfield, Dublin 4, Ireland, and UCD Earth Institute, University College  
13 Dublin, Belfield, Dublin 4, D04 V1W8, Ireland.

14 5. School of Physical Sciences, The Open University, Walton Hall, Milton  
15 Keynes MK7 6AA, UK

16 \*. Corresponding Authors: NA: nsa12@cam.ac.uk. FEGB:  
17 f.butcher@sheffield.ac.uk

18 **Bright radar reflections observed at the Ultimi Scopuli region of**  
19 **Mars' south polar layered deposits (SPLD) <sup>1,2,3</sup> by the Mars**  
20 **Advanced Radar for Subsurface and Ionosphere Sounding**  
21 **(MARSIS) instrument have been interpreted as the signature of**  
22 **areas of subglacial water beneath it. However, other studies put**  
23 **forward alternative explanations that do not imply the presence of**  
24 **liquid water<sup>4,5,6</sup>. Here we shed light on the issue by looking at the**  
25 **surface topography of the region. On Earth, reduced or absent**  
26 **basal friction, and consequent ice velocity changes, cause a**  
27 **distinct topographic signature over subglacial lakes<sup>7</sup>. Using Mars**  
28 **Orbiter Laser Altimeter (MOLA) data, <sup>8</sup> we identify and**  
29 **characterise an anomaly in the surface topography of the SPLD**  
30 **overlying the area of the putative lakes, similar to those found**  
31 **above terrestrial subglacial lakes of similar size. Ice flow model**  
32 **results suggest comparable topographic anomalies form within**  
33 **0.5 – 1.5 Myr with locally elevated geothermal heating<sup>9</sup> or 2 – 5**  
34 **Myr without elevated geothermal heating<sup>2</sup>. These findings offer**  
35 **independent support for the presence of basal water beneath**

36 **Ultimi Scopuli and suggest surface topography could supplement**  
37 **radar returns to help identify other potential subglacial water**  
38 **bodies.**

39 Main

40 Ice deposits on planetary surfaces raise the temperature at the  
41 ice/bedrock interface, as geothermal heat must be conducted through the  
42 ice rather than being lost directly at the bedrock surface. Frictional heat  
43 produced by flowing ice is concentrated at the base of the ice mass<sup>10</sup>,  
44 further warming the ice/bedrock interface. On Earth, many glacier beds  
45 reach the pressure melting point, and subglacial lakes are widespread;  
46 hundreds have been identified beneath the Antarctic Ice Sheet<sup>11</sup>, and  
47 over 50 beneath the Greenland ice sheet<sup>11</sup>. Whilst there is evidence for  
48 past subglacial water beneath an ancient south polar ice sheet on  
49 Mars<sup>12,13</sup>, and more recent water (100s Myr ago) beneath some existing  
50 mid-latitude ice deposits<sup>14,10,15,23</sup>, it is widely assumed that Mars' present-  
51 day ice deposits are frozen throughout under cold, dry contemporary  
52 climate conditions.

53 This assumption has been questioned by the areas of bright basal radar  
54 reflections in MARSIS data from Ultimi Scopuli, centred around 81°S,  
55 193°E (Fig. 1a), which have been taken to be indicative of one<sup>1</sup>, or  
56 multiple<sup>2</sup> subglacial water bodies (likely in the form of saturated  
57 perchlorate brines<sup>1,2,9,16</sup>). Additional areas of high basal reflected radar  
58 power across the SPLD<sup>3</sup> also potentially indicate more widespread basal  
59 water. The liquid water explanation for the bright radar reflections is  
60 contested, however. Local changes in the electrical conductivity of the  
61 substrate could be a cause<sup>4</sup>, potentially due to liquid brines, metal-  
62 bearing minerals, saline ice, or cold, hydrated smectite clays<sup>5</sup>. Such  
63 deposits occur in the highlands surrounding the SPLD, and are argued to  
64 be likely to occur, and be detectable, beneath the SPLD<sup>4,5,6</sup>. However,  
65 analyses of the MARSIS data alone have not confirmed either a liquid or  
66 solid interpretation for the bright basal radar reflections.

67 Subglacial lakes are commonly identified on Earth using ice penetrating  
68 radar. However, a small number have been identified by their influence  
69 on the surface topography<sup>7,17,18</sup>. Reduced basal friction and consequent  
70 ice velocity changes over basal water (particularly lakes) lead to the  
71 development of flat areas on ice surfaces over large lakes (e.g. Lake  
72 Vostok), with extensional flow at the upstream margin causing surface  
73 lowering, and compressional flow at the downstream margin causing a

74 surface rise<sup>7</sup>. Smaller lakes (~10 – 20 km in size) seem not to develop  
75 the large flat area, but still show a distinctive undulation along the ice  
76 flowline over the lake<sup>7</sup>.

77 Here, we have identified a local anomaly in the Mars Orbiter Laser  
78 Altimeter (MOLA) SPLD surface topography<sup>8</sup> over the area of inferred  
79 subglacial water in Ultima Scopuli<sup>1</sup>. The regional MOLA topography (Fig.  
80 1b) is generally planar away from a surface depression ~60 km to the  
81 south of the inferred water, and the large asymmetric polar scarps  
82 (LAPS<sup>19</sup>) ~30 km to the north-west. The general topographic trend is a  
83 gentle slope (~0.15°) towards the ice edge to the north-east (average  
84 azimuth ~66° clockwise from N). However, topographic analysis  
85 techniques sensitive to subtle, local variations (Methods) show a clear  
86 anomaly proximal to the inferred water bodies. Slope-shading<sup>20</sup> reveals a  
87 distinct feature (white arrows in Fig. 1c) trending through the centre of  
88 the region towards the LAPS to the north-west. Linear trend surface  
89 analysis over the central 30 km radius area shows a strong fit ( $R^2 =$   
90  $0.994$ ,  $P < 10^{-6}$ ), but with significant spatial autocorrelation (Moran's  $I =$   
91  $0.972$ ,  $P < 0.001$ ) in the residuals (Fig. 1d). There is a raised WNW-ESE-  
92 oriented 'bench' (a, Fig. 1d) up to 7 m above the trend surface, located  
93 just off-centre to the ESE of the area of inferred water<sup>1</sup>, with an  
94 associated topographic depression up to 4 m below the trend surface (b,  
95 Fig. 1d) ~10 – 15 km up-slope of the bench. There are also two local lows  
96 near the E and SW edges of the region (c and d, Fig. 1d); the residuals  
97 near the NW edge of the area are affected by the nearby LAPS (yellow  
98 arc, Fig 1d). Contributing area algorithm<sup>21</sup> results (Fig. 1e) show a clear  
99 diversion in the steepest downhill slope direction near the centre of the  
100 region due to the presence of the bench and depression.

101 The height differences from the regional trend over the bench and  
102 depression, along the ice flow direction, are very similar to those  
103 observed (~ +/- 5 – 10 m) over small (10 – 20 km diameter) Antarctic  
104 lakes<sup>7</sup>. They are small compared with the overall elevation range of ~200  
105 m across the 30 km radius area, but given the vertical precision of the  
106 MOLA instrument (<1 m)<sup>8</sup> and low overall slopes in the area, our analysis  
107 shows that they alter the local surface elevation, slope and aspect  
108 sufficiently to appear both as coherent areas of similar trend surface  
109 residuals and to cause the clear deviation in the direction of steepest  
110 slope seen in the contributing area results. By contrast, the depressions  
111 visible in the residuals at the edge of the area (Fig. 1d c and d) do not  
112 affect contributing area results.

113 Given the cold temperature of the SPLD and lower Martian gravity, the  
114 question remains as to whether absent basal friction over water bodies  
115 could lead to a surface topographic effect, or if flow is too slow, or the ice  
116 too thick, for a detectable effect. To assess the possibility that the  
117 anomalies reported here could result from subglacial water, we conducted  
118 a series of experiments using a high-order numerical ice flow model, the  
119 Ice Sheet and Sea Level System Model (ISSM<sup>22</sup>, Methods) allowing basal  
120 sliding over the inferred water bodies<sup>1,2</sup>. Given the likely influence of  
121 MARSIS radar track orientation and spacing on inferred shape and extent  
122 of the inferred water areas, we also conduct experiments with two  
123 synthetic shapes: a circular water body 10 km in radius (similar in size to  
124 the first-identified water body<sup>1</sup>), and a lozenge-shaped water body  
125 located just up-ice of the topographic bench, and of comparable shape  
126 and area (Methods). The generation of subglacial water within the region  
127 probably required locally elevated geothermal flux (GHF)<sup>9,23</sup>, which affects  
128 ice viscosity and thus ice flow. We explored the effect of GHF varied  
129 between a nominal background value (30 mWm<sup>-2</sup>) and a maximum of 90  
130 mWm<sup>-2</sup>, over a variable radius (20 – 40 km) area surrounding the  
131 inferred water body(-ies). This encompasses the range of GHF anomalies  
132 investigated by Sori and Bramson<sup>9</sup>, exceeding the 72 mWm<sup>-2</sup> they find  
133 necessary to raise the basal ice to ~200K, just above the lowest melting  
134 point among the saturated perchlorate brine species (Ca) they  
135 investigate. Details of all model runs are given in Supplementary Table 1.

136 Model results (Fig. 2) show that altered basal friction and/or elevated GHF  
137 can produce changes in surface topography, comparable to those  
138 observed, within 500 kyr – 1.5 Myr. This is similar to the modelled  
139 duration of local GHF elevation due to magma chamber emplacement<sup>9</sup>.  
140 We find a GHF of 60 mWm<sup>-2</sup> is the minimum needed to raise the modelled  
141 basal temperature to ~200K, lower than the 72 mWm<sup>-2</sup> reported by Sori  
142 and Bramson<sup>9</sup>, due to the additional effect of strain-induced heating  
143 under enhanced flow<sup>10</sup>. We therefore focus mainly on model runs using 60  
144 mWm<sup>-2</sup> GHF as this requires the smallest heat anomaly.

145 Elevation changes of ~ +/- 5 m occur in 500 kyr in the largest central  
146 area of inferred water<sup>2</sup> with the highest GHF, 90 mWm<sup>-2</sup>, applied over a  
147 40 km radius (Fig. 2a; Run M1, Supplementary Table 1). Elevation  
148 changes of ~ +/- 3 m are produced in 1.5 Myr when sliding is allowed  
149 over the single water body<sup>1</sup>, with 60 mWm<sup>-2</sup> GHF over a 20 km radius  
150 (Fig. 2b, Run S9). The synthesised 10 km radius circular water area gives  
151 elevation changes of ~ +/- 5 m in 1 Myr with 60 mWm<sup>-2</sup> GHF over a  
152 30 km radius (Fig 2c, Run C3). With 60 mWm<sup>-2</sup> GHF over an expanded

153 lozenge-shaped area equivalent in area to a 30km radius circle  
154 (Methods), the synthesised lozenge-shaped water area produces  $\sim \pm 4$   
155 m elevation changes in 1 Myr (Fig. 2d, Run LL6). Without additional GHF,  
156 allowing basal sliding over the inferred water is sufficient for surface  
157 elevation changes of comparable magnitude to those observed to occur  
158 within 2 – 5 Myr. The shape of the modelled water (zero friction) area  
159 strongly influences the shape of the area in which elevation changes  
160 occur; the amount of surface elevation change scales with the area of  
161 altered friction, and with the magnitude and spatial extent of additional  
162 GHF (Supplementary Information).

163 Figure 3 shows scatter diagrams of the trend surface residuals (Fig. 1d)  
164 versus modelled elevation changes for the runs in Figure 2 for the 824  
165 model grid points within a 20 km radius of the centre of the inferred wet  
166 area(s). All models produce significant relationships;  $R^2$  values vary  
167 between 0.05 (Run M1) and 0.49 (Run LL6). The  $R^2$  values are affected  
168 by areas away from the inferred water areas which exhibit very low  
169 modelled elevation change, but have non-zero residuals, visible as  
170 horizontal clusters of points in Figure 3. The correspondence between the  
171 edges of the high radar reflectance areas and the orientation and spacing  
172 of the MARSIS satellite tracks in the region also suggest that the edges of  
173 the inferred water bodies are uncertain, affecting the spatial  
174 correspondence between model results and the surface topographic  
175 anomaly.

176 The higher predictive power of models with a single area of inferred  
177 water, compared to the model with multiple inferred water bodies,  
178 suggests that a single area of water best matches the topographic  
179 anomaly. Other than for model run M1, the smaller modelled elevation  
180 changes in Fig. 2 compared with the topographic anomaly, and shallower  
181 than 1:1 relationships in Fig. 3, suggest either  $\text{GHF} > 60 \text{ mWm}^{-2}$  may be  
182 needed, or that GHF may need to remain elevated for  $> 1$  Myr.

183 Given the excellent regional MOLA point coverage (Methods), the fact that  
184 the anomaly is unique in spatial coherence and extent in the area  
185 investigated suggests it is not a data artifact, but a real feature. The  
186 anomaly is located very close to the largest<sup>2</sup> and first identified<sup>1</sup> inferred  
187 water body, which shows the brightest radar reflections, highest acuity,  
188 and dielectric permittivity, making its interpretation as liquid the most  
189 secure. The elongate shape of the anomaly, and best statistical match for  
190 model run LL6, may suggest the geothermal heat source could have a  
191 more linear shape, as would be associated with an igneous dyke. A

192 difference in water-body shape from that suggested by the radar returns  
193 is likely due to uncertainties in the true edge position of the high radar  
194 reflectance areas due to MARSIS track orientation and spacing.

195 The rates of elevation change we find are low (peak values of  $< 0.02$   
196  $\text{mmyr}^{-1}$ ), but given the large uncertainties in SPLD surface age estimates  
197 ( $\sim 10\text{s Myr} - \sim 100\text{s Myr}^{24,25}$ ), they could sufficiently influence the  
198 topography over the time period suggested for elevated geothermal  
199 heating due to magma emplacement<sup>9</sup>.

200 Our results suggest that analysis of Mars' SPLD surface topography could  
201 assist in identifying which areas of bright radar reflections<sup>3</sup> in MARSIS  
202 data could be explained by subglacial water bodies, and which may be  
203 due to solid materials. If other areas of bright radar reflections show no  
204 topographic anomaly, this could make a general explanation for high  
205 reflected radar power based on different solid materials more likely. This  
206 would make Ultimi Scopuli unique in containing both bright basal radar  
207 reflections<sup>1,2</sup> and a surface topographic signature indicative of an area of  
208 zero basal friction. If other areas of bright radar reflections also show  
209 surface topographic changes, it may be that basal water occurs more  
210 commonly beneath the SPLD, making the long-term presence of brines at  
211 sub-eutectic temperatures a possible explanation<sup>2</sup>.

212 Our analysis of the surface topography over an area of subglacial water  
213 inferred from MARSIS data shows the first evidence for subglacial water  
214 beneath Mars' SPLD that is independent of MARSIS data. Through the  
215 combination of the topographic anomaly we identify, numerical model  
216 experiments showing the impact of subglacial water on surface  
217 topography, and the MARSIS data itself, our results suggest subglacial  
218 liquid water generated by local geothermal heating is the most likely  
219 explanation for the bright basal radar returns in the Ultima Scopuli area of  
220 Mars' SPLD.

## 221 Methods

### 222 *Topographic analysis*

223 For all topographic analyses, we use the Mars Orbiter Laser Altimeter  
224 (MOLA) surface topography for the south polar region at a resolution of  
225 256 pixels per degree ( $\sim 230\text{m}$  ground resolution)<sup>8</sup>. We checked the MOLA  
226 point distribution in the study area; the tracks ran both normal and  
227 parallel to the anomaly, and the largest point-to-point spacing is very  
228 similar to the DEM grid size. Thus, we expect the DEM to be free of  
229 interpolation errors in the study area.

### 230 *Slope shading*

231 Slope-shading, in which subtle shading depending on local slope and  
232 aspect is added to contour maps, is commonly used to emphasise relief to  
233 aid visual interpretation of elevation data. We calculate a shading value  
234 ( $\zeta$ ) from the local surface slope ( $S$ ) and aspect ( $A$ ), and the inclination ( $I$ )  
235 and declination ( $D$ ) of the assumed illumination vector following  
236 Kennelly<sup>20</sup>.

$$237 \quad \zeta = \cos(I) \sin(S) \cos(A-D) + \sin(I) \cos(S) \quad (1)$$

238 We illuminate the image from the left of the DEM as shown in the figures,  
239 at an angle of  $30^\circ$  above horizontal, and apply a 2.5 x vertical  
240 exaggeration.

### 241 *Trend Surface Analysis*

242 To quantify local elevation deviations from an assumed regional surface,  
243 we fit a linear trend surface for MOLA elevation, using polar stereographic  
244 grid coordinates, over the area within a 30 km radius of the centre of the  
245 inferred water body<sup>1</sup> in order to minimise the influence of the LAPS on the  
246 trend surface, and focus on the area containing the inferred water bodies.  
247 Residual values show deviations from the trend surface, with negative  
248 values showing local lowering. To show spatial autocorrelation in the  
249 residuals we calculate Moran's  $I$ , using a simple 8-neighbour adjacency  
250 matrix with horizontal and vertical weights set to 1, and corner weights  
251 set to  $1/\sqrt{2}$ .

### 252 *Contributing Area*

253 We use a contributing area algorithm to demonstrate deviations in surface  
254 topography; such algorithms are commonly used in hydrological analysis  
255 of topography. Each cell in the surface DEM is assigned a value based on  
256 its own area, plus the total area of all cells upslope of the original cell for  
257 which the lines of steepest descent pass through the cell. The algorithm

258 we use<sup>21</sup> passes its calculated area to the single steepest downhill cell  
259 (known as a D8 algorithm) and preserves connectivity through closed  
260 depressions in the DEM by identifying the lowest cell in the ridge  
261 surrounding any closed depressions within the DEM, and routing the area  
262 feeding such depressions over this spill-point into the next cell downslope.  
263 Contributing area algorithms clearly identify the main potential drainage  
264 axes within the topography, as contributing area values at the bottom of  
265 valleys (where river channels would be expected to be located on Earth)  
266 are much larger than the surrounding cells on valley sides or ridges. The  
267 route of such drainage axes is very sensitive to changes in the local slope  
268 and aspect.

### 269 *Ice Flow Modelling*

270 We use the Ice Sheet and Sea Level System Model (ISSM<sup>22</sup>) to model ice  
271 flow. This is a fully-thermomechanically coupled, finite-element, higher  
272 order ice flow model which can be used in a variety of modes of  
273 increasing complexity. For our experiments, we use the implementation of  
274 the Blatter-Pattyn simplifications of the Stokes Equations within ISSM<sup>22</sup>.  
275 Initial experiments showed no discernible difference between this  
276 simplification and a full solution to the Stokes equations, but made a  
277 considerable saving in computing time, enabling a larger suite of runs to  
278 be performed. We use the MOLA topography (as above) for the ice sheet  
279 surface, and the Mars Advanced Radar from Subsurface and Ionosphere  
280 Sounding (MARSIS) basal topography<sup>26</sup>, supplemented in the region of  
281 the water bodies by the 'mean perturbed' topography from Arnold et al.<sup>23</sup>

282 We define the model domain by identifying the ice divide surrounding the  
283 area containing the water bodies using the contributing area algorithm.  
284 We identify all cells within the area covered by the late Amazonian polar  
285 cap (IApc) unit<sup>27</sup> for which the line of steepest descent passes through the  
286 area containing the water bodies, and the cells downstream, in a similar  
287 way to a modelling study of ice flow over Lake Vostok, Antarctica<sup>28</sup>. Mesh  
288 resolution is set to 1 km within 30 km of the location of the water bodies,  
289 and 10 km elsewhere. Model parameters are given in Supplementaty  
290 Table 2.

291 To initialise the model, we first perform a steady-state calculation of the  
292 stress balance and resulting ice velocity within the model domain  
293 assuming the ice is at the surface temperature throughout, with zero  
294 basal sliding allowed. The calculated isothermal velocity is then used as  
295 an input into a steady-state, thermally coupled run which is used to  
296 calculate the steady-state temperature within the domain. This calculates

297 the basal temperature, and allows for the softening effect of geothermal  
298 heat and internal strain heating on the ice. Given the uncertainty in the  
299 SPLD surface mass balance, these runs assume zero surface mass  
300 balance. We then use the temperature and ice velocity results of the  
301 steady-state, thermally coupled run as additional input values in a  
302 transient (time-dependent) run for 1000 model years, again with zero  
303 surface mass balance. We use the negative of modelled surface height  
304 change over this period as the assumed surface mass balance (so a  
305 surface lowering becomes a positive mass balance and vice versa) in the  
306 subsequent main model experiments to eliminate as far as possible any  
307 background flow-induced effect on the long-term evolution of the surface  
308 topography. Modelled changes in surface topography in the main  
309 experiments are therefore due to changes in ice flow induced by the  
310 assumed basal friction and/or geothermal heat flux changes. Model basal  
311 topography and ice thickness data, and the calculated steady-state basal  
312 temperature, ice velocity and implied surface mass balance used to  
313 initialise the dynamic runs, are shown in Supplementary Figure 1.

314 For the main model experiments, we allow basal sliding (using the  
315 standard basal friction parameterization in ISSM, setting the friction  
316 coefficient to zero, implicitly assuming the water body is deep enough to  
317 completely detach the basal ice from the bed) over the inferred area of  
318 basal water for each model run. We perform four main sets of  
319 experiments. 'M' runs allow sliding over the areas with dielectric  
320 permittivity  $> 15$  digitised from Figure 5 in Lauro et al.<sup>2</sup>; 'S' runs allow  
321 sliding over the area digitised from the area of positive normalised basal  
322 echo power identified by Orosei et al.<sup>1</sup>, Figure 3B. The MARSIS radar  
323 track spacing and orientation likely influence the spatial interpolation of  
324 the inferred areas of liquid (shown by the correspondence between the  
325 edges of the high radar reflectance areas identified and the orientation of  
326 the satellite tracks in the region), potentially affecting their inferred  
327 shape. Therefore, we also perform a set of runs with a synthetic circular  
328 area (radius 10 km) of zero friction ('C runs'), centred over the similarly-  
329 sized high radar reflectance area identified by Orosei et al.<sup>1</sup>, and with a  
330 lozenge-shaped area of zero friction ('L runs') based on the shape and  
331 area of the topographic bench we identify (Fig. 1c), offset by 5 km up-ice.  
332 Outlines of the inferred zero-friction areas can be seen in Figure 2. We  
333 also apply a local elevated geothermal heat flux in a variable radius (20  
334 km to 40 km) area centred on the inferred water bodies, up to a  
335 maximum value of  $90 \text{ mWm}^{-2}$ , covering the range of heat fluxes required  
336 to achieve basal melt, as modelled by Sori and Bramson<sup>9</sup>. For run LL6 we  
337 use an enlarged lozenge shaped area of elevated geothermal heating with

338 equivalent area to a 30km radius circular area (Fig. 2d). Additional model  
339 outputs for Runs M1 and S9 (Figs. 2a-b and 3a-b) are shown in  
340 Supplementary Figure 2.

341 Model duration is initially set to 1 Myr, but for runs with spatially-limited  
342 basal sliding and/or lower geothermal heat we extend this to 10 Myr. We  
343 undertook some additional 'C' runs to investigate the assumed ice density  
344 and thermal conductivity (reflecting the uncertainty in these values, and  
345 the range used in other modelling studies of Martian ice masses). We also  
346 performed two runs with no sliding, with and without additional  
347 geothermal heating; the latter run allowing us to check any possible  
348 influence of ice flow alone on topography. Full details of the model runs  
349 are given in Supplementary Table 1, and additional details of model  
350 inputs and results are given in the Supplementary Information and  
351 Supplementary Figures 1 - 2.

## 352 Data Availability

353 MOLA and MARSIS data are available from the PDS Geosciences node  
354 at <http://pds-geosciences.wustl.edu/missions/mgs/megdr.html> and at  
355 [https://pds-geosciences.wustl.edu/missions/mars\\_express/marsis.htm](https://pds-geosciences.wustl.edu/missions/mars_express/marsis.htm)  
356 respectively; MARSIS data are also available at the ESA Planetary Science  
357 Archive ([https://archives.esac.esa.int/psa/#!Ta-](https://archives.esac.esa.int/psa/#!Ta-ble%20View/MARSIS=instrument)  
358 [ble%20View/MARSIS=instrument](https://archives.esac.esa.int/psa/#!Ta-ble%20View/MARSIS=instrument)). The 'mean perturbed' bed  
359 topography<sup>23</sup> data used in the area containing the inferred water bodies is  
360 available via the University of Cambridge Apollo repository at  
361 <https://doi.org/10.17863/CAM.41622>.

## 362 Code Availability

363 ISSM is available from NASA/JPL at <https://issm.jpl.nasa.gov>. Code used  
364 to calculate slope shading and contributing area are available by  
365 reasonable request to the corresponding author.

## 366 Acknowledgements

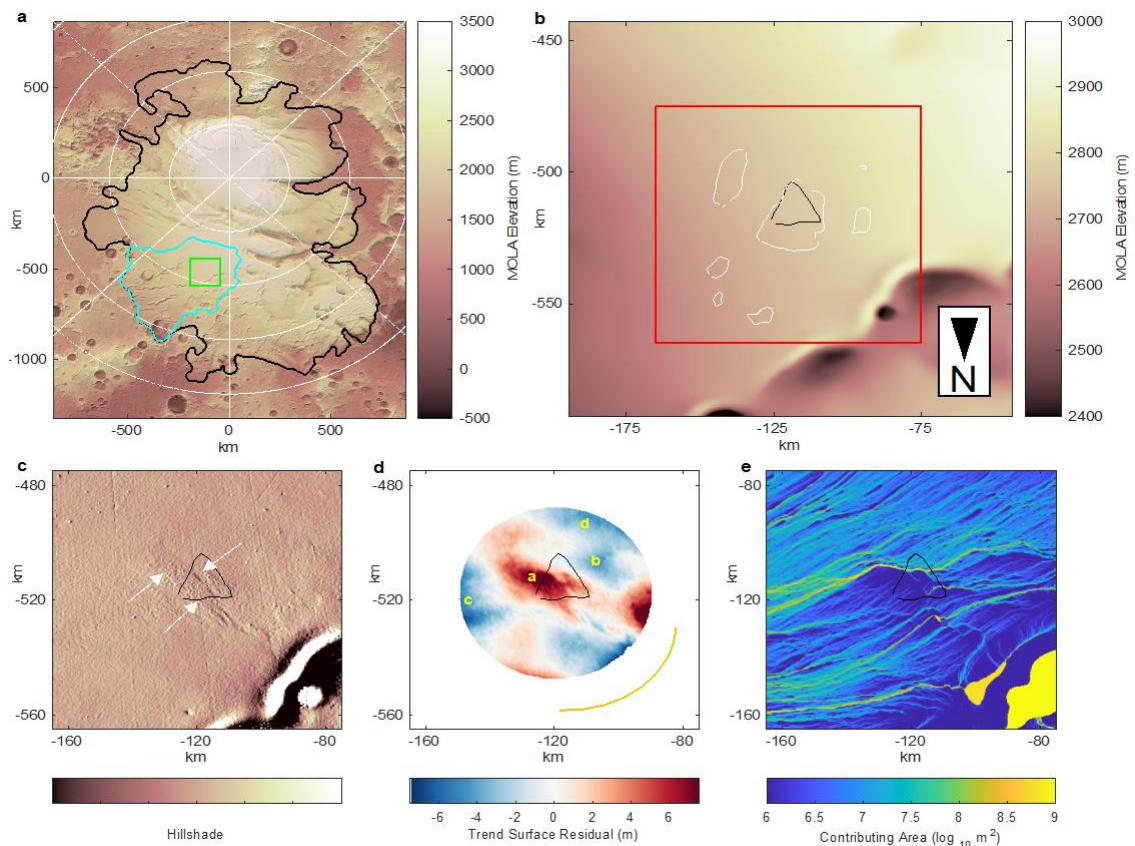
367 The MARSIS instrument and experiment were funded by the Italian Space  
368 Agency and NASA. It was developed by the University of Rome, Italy, in  
369 partnership with NASA's Jet Propulsion Laboratory [JPL], Pasadena, CA.  
370 The Mars Express and Mars Global Surveyor missions are operated by the  
371 space agencies of Europe (European Space Agency), Italy (Agenzia  
372 Spaziale Italiana) and the United States (NASA). FB is part of the  
373 PALGLAC team of researchers and received funding from the European  
374 Research Council (ERC) under the European Union's Horizon 2020  
375 research and innovation programme (Grant agreement No. 787263). We  
376 thank Mathieu Morlighem for help and discussions with ISSM installation  
377 and setup.

## 378 Author Contribution

379 Topographic analysis and modelling was undertaken by NA. FB and SC  
380 assisted with MOLA and MARSIS data download and processing, and with  
381 initial discussions on the possibility of detecting surface anomalies on the  
382 SPLD. CG and MB extracted and processed the original MOLA point data  
383 from the repository and checked coverage in the study area. The initial  
384 draft of the MS was written by NA; all authors contributed to the  
385 submitted version, revisions, and to discussions on the aims and  
386 arguments within the paper.

387 Competing Interests

388 The authors declare no competing interests.

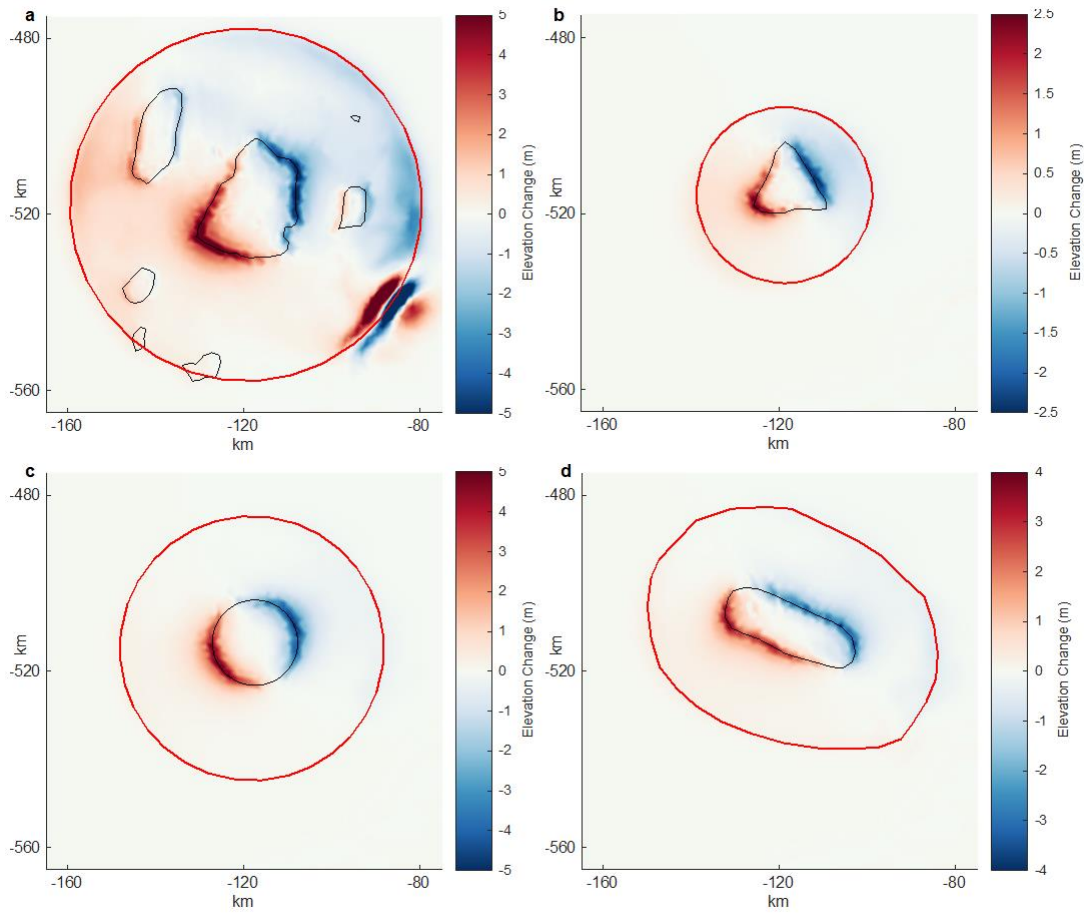


390

391 **Figure 1. Surface topography of Mars' South Polar Layered**  
 392 **Deposit, and topographic analysis results.** **a.** Regional SPLD MOLA  
 393 Topography<sup>8</sup>. Black outline shows the outline of the late Amazonian polar  
 394 cap (IAPc) unit<sup>27</sup>. Cyan outline shows model domain (Methods); green  
 395 outline shows the region containing the inferred subglacial water bodies  
 396 shown in **b**. **b.** MOLA topography of the area shown by the green box in **a**.  
 397 Black outline shows the single inferred subglacial water body<sup>1</sup> and the  
 398 white outlines show the inferred multiple water bodies<sup>2</sup>. Red square  
 399 denotes the area shown in **c** and **d**. **c.** Hill-shade (Methods) of the area  
 400 shown by the red square in **b**. White arrows show the topographic  
 401 anomaly. **d.** Residuals from linear trend surface analysis over the 30 km  
 402 radius region centred on the inferred water area. Letters a to d show  
 403 areas of spatially autocorrelated residuals discussed in the text. Yellow arc  
 404 shows the location of the nearby LAPS. Black outline as **b**. **e.** Contributing  
 405 area map (see Methods) showing the surface area upstream of any given  
 406 point. Black outline as **b**. The main axes of high contributing area (yellow)  
 407 deviate from the general regional north-easterly direction by kinking  
 408 around the area of positive residuals (a in panel c) before reverting to the  
 409 regional trend down-slope. Yellow areas in the NW are due to topographic

410 lows associated with the LAPS. Maps use MOLA polar stereographic  
411 projection data at 256 pixels per degree ( $\sim 230$  m per pixel); X and Y axis  
412 labels are coordinates in km. Note that for b – e, north is towards the  
413 bottom edge, comparable with figures in Orosei et al.<sup>1</sup> and Lauro et al.<sup>2</sup>

414



415

416

417

418

419

420

421

422

423

424

425

426

427

428

429

430

431

432

433

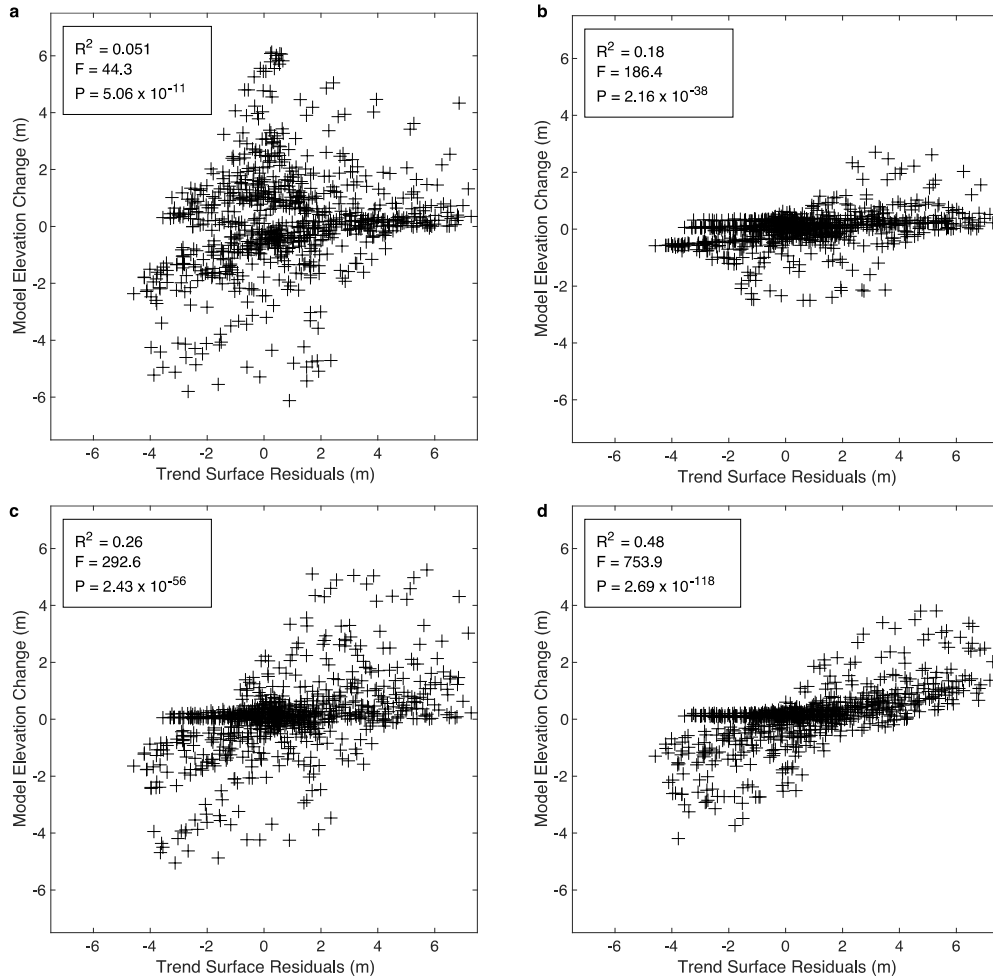
434

435

**Figure 2. Model results for the centre of the region containing the inferred water** (red box in Fig. 1b). **a.** Results from run M1 (Methods) allowing basal sliding over multiple water bodies<sup>2</sup> (black outlines), with 90 mWm<sup>-2</sup> GHF over a 40km radius (red outline), after 500,000 model years. Maximum rate of change in elevation of + 1.7x10<sup>-5</sup> myr<sup>-1</sup> / - 1.7x10<sup>-5</sup> myr<sup>-1</sup> is reached ~ 150 kyr after the onset of heating. The effect of temperature-induced softening of the ice due to high GHF can be seen around the edge of the heated area, with surface lowering up-slope and surface raising down-slope. The large height changes in the NW corner are due to the increase in ice velocity caused by softening over the steep slopes of the LAPS. **b.** Results from run S9 allowing sliding over the single central water body<sup>1</sup> (black outline), with 60 mWm<sup>-2</sup> GHF over a 20 km radius (red outline) after 1 Myr. Maximum rate of elevation change of + 1.7x10<sup>-6</sup> myr<sup>-1</sup> / - 1.7x10<sup>-6</sup> myr<sup>-1</sup> occurs ~ 200 kyr after the onset of heating. **c.** Results from run C6 allowing sliding over a 10km radius circular region (black outline), with 60 mWm<sup>-2</sup> GHF over a 30 km radius area (red line) after 1 Myr. Maximum rate of elevation change of + 4.8 x10<sup>-6</sup> myr<sup>-1</sup> / - 4.6x10<sup>-6</sup> myr<sup>-1</sup> occurs ~ 200kyr after the onset of heating. **d.** Results from run LL6 allowing sliding over a lozenge-shaped water body (black outline), with 60 mWm<sup>-2</sup> GHF applied within red outline

436 (Methods). Maximum rate of elevation change of  $+ 3.3 \times 10^{-6} \text{ myr}^{-1}$  / -  
437  $3.6 \times 10^{-6} \text{ myr}^{-1}$  occurs  $\sim 200 \text{ kyr}$  after the onset of heating. X and Y axes,  
438 and figure orientation as Fig. 1.

439



440

441 **Figure 3. Scatter plots of residuals from trend surface shown in**  
 442 **Figure 1d against modelled elevation changes within 20 km radius**

443 **of the centre of the region containing the inferred water.** Trend

444 surface residuals are at the nearest MOLA grid point to modelled grid

445 points. **a.** Run M1. **b.** Run S9. **c.** Run C6. **d.** Run LL6. Ordinary least

446 squares regression results for modelled height change versus trend

447 surface residuals are given as the  $R^2$  statistic, the F statistic for a

448 significant linear regression relationship, and the P-value for F. In all

449 cases,  $n = 824$ ,  $DF = 822$ .

## 450 References

- 451 1. Orosei, R. *et al.* Radar evidence of subglacial liquid water on Mars.  
452 *Science* **361**, 490–493 (2018).
- 453 2. Lauro, S. E. *et al.* Multiple subglacial water bodies below the south pole  
454 of Mars unveiled by new MARSIS data. *Nat. Astron.* **5**, 63–70 (2021).
- 455 3. Khuller, A. R. & Plaut, J. J. Characteristics of the Basal Interface of the  
456 Martian South Polar Layered Deposits. *Geophys. Res. Lett.* (2021)  
457 doi:10.1029/2021GL093631.
- 458 4. Bierson, C. J., Tulaczyk, S., Courville, S. W. & Putzig, N. E. Strong  
459 MARSIS Radar Reflections from the Base of Martian South Polar Cap  
460 may be due to Conductive Ice or Minerals. *Geophys. Res. Lett.* (2021)  
461 doi:10.1029/2021GL093880.
- 462 5. Smith, I. B. *et al.* A Solid Interpretation of Bright Radar Reflectors  
463 Under the Mars South Polar Ice. *Geophys. Res. Lett.* (2021)  
464 doi:10.1029/2021GL093618.
- 465 6. Grima, C., Mouginot, J., Kofman, W., Hérique, A. & Beck, P. The Basal  
466 Detectability of an Ice-Covered Mars by MARSIS. *Geophys. Res. Lett.*  
467 **49**, (2022).
- 468 7. Ridley, J. K., Cudlip, W. & Laxon, S. W. Identification of subglacial lakes  
469 using ERS-1 radar altimeter. *J. Glaciol.* **39**, 625–634 (1993).
- 470 8. Smith, D. E. *et al.* Mars Orbiter Laser Altimeter: Experiment summary  
471 after the first year of global mapping of Mars. *J. Geophys. Res. Planets*  
472 **106**, 23689–23722 (2001).
- 473 9. Sori, M. M. & Bramson, A. M. Water on Mars, with a grain of salt: local  
474 heat anomalies are required for basal melting of ice at the south pole  
475 today. *Geophys. Res. Lett.* **46**, 1222–1231 (2019).
- 476 10. Butcher, F. E. G. *et al.* Recent basal melting of a mid-latitude glacier  
477 on Mars. *J. Geophys. Res. Planets* **122**, 2445–2468 (2017).
- 478 11. Livingstone, S. J. *et al.* Subglacial lakes and their changing role in a  
479 warming climate. *Nat. Rev. Earth Environ.* **3**, 106–124 (2022).
- 480 12. Butcher, F. E. G., Conway, S. J. & Arnold, N. S. Are the Dorsa  
481 Argentea on Mars eskers? *Icarus* **275**, 65–84 (2016).
- 482 13. Head, J. W. & Pratt, S. Extensive Hesperian-aged south polar ice  
483 sheet on Mars: Evidence for massive melting and retreat, and lateral  
484 flow and ponding of meltwater. *J. Geophys. Res. Planets* **106**, 12275–  
485 12299 (2001).
- 486 14. Gallagher, C. & Balme, M. Eskers in a complete, wet-based glacial  
487 system in the Phlegra Montes region, Mars. *Earth Planet. Sci. Lett.* **431**,  
488 96–109 (2015).

- 489 15. Butcher, F. E. G. *et al.* Sinuous ridges in Chukhung crater, Tempe  
490 Terra, Mars: Implications for fluvial, glacial, and glaciofluvial activity.  
491 *Icarus* **357**, 114131 (2021).
- 492 16. Mattei, E. *et al.* Assessing the role of clay and salts on the origin of  
493 MARSIS basal bright reflections. *Earth Planet. Sci. Lett.* **579**, 117370  
494 (2022).
- 495 17. Remy, F., Mazzega, P., Houry, S., Brossier, C. & Minster, J. F.  
496 Mapping of the Topography of Continental Ice by Inversion of Satellite-  
497 altimeter Data. *J. Glaciol.* **35**, 98–107 (1989).
- 498 18. Mantripp, D. N., Ridley, J. K. & Rapley, C. G. Antarctic map from the  
499 Geosat Radar Altimeter Geodetic Mission. *Earth Obs. Quarterly* **37–38**,  
500 6–10 (1992).
- 501 19. Grima, C. *et al.* Large asymmetric polar scarps on Planum Australe,  
502 Mars: Characterization and evolution. *Icarus* **212**, 96–109 (2011).
- 503 20. Kennelly, P. J. Terrain maps displaying hill-shading with curvature.  
504 *Geomorphology* **102**, 567–577 (2008).
- 505 21. Arnold, N. A new approach for dealing with depressions in digital  
506 elevation models when calculating flow accumulation values. *Prog.*  
507 *Phys. Geogr. Earth Environ.* **34**, 781–809 (2010).
- 508 22. Larour, E., Seroussi, H., Morlighem, M. & Rignot, E. Continental  
509 scale, high order, high spatial resolution, ice sheet modeling using the  
510 Ice Sheet System Model (ISSM). *J. Geophys. Res. Earth Surf.* **117**,  
511 (2012).
- 512 23. Arnold, N. S., Conway, S. J., Butcher, F. E. G. & Balme, M. R.  
513 Modeled Subglacial Water Flow Routing Supports Localized Intrusive  
514 Heating as a Possible Cause of Basal Melting of Mars' South Polar Ice  
515 Cap. *J. Geophys. Res. Planets* **124**, 2101–2116 (2019).
- 516 24. Herkenhoff, K. Surface Ages and Resurfacing Rates of the Polar  
517 Layered Deposits on Mars. *Icarus* **144**, 243–253 (2000).
- 518 25. Koutnik, M., Byrne, S. & Murray, B. South Polar Layered Deposits of  
519 Mars: The cratering record: SOUTH POLAR LAYERED DEPOSITS OF  
520 MARS. *J. Geophys. Res. Planets* **107**, 10-1-10–10 (2002).
- 521 26. Plaut, J. J. *et al.* Subsurface radar sounding of the south polar  
522 layered deposits of Mars. *Science* **316**, 92–95 (2007).
- 523 27. Tanaka, K. L. *et al.* *Geologic map of Mars*. 48  
524 <http://pubs.er.usgs.gov/publication/sim3292> (2014).
- 525 28. Pattyn, F., Smedt, B. D. & Souchez, R. Influence of subglacial  
526 Vostok lake on the regional ice dynamics of the Antarctic ice sheet: a  
527 model study. *J. Glaciol.* **50**, 583–589 (2004).
- 528 29. Fisher, D. A., Hecht, M. H., Kounaves, S. P. & Catling, D. C. A  
529 perchlorate brine lubricated deformable bed facilitating flow of the north

530 polar cap of Mars: Possible mechanism for water table recharging. *J.*  
531 *Geophys. Res.* **115**, (2010).  
532

## Supplementary Information for “Surface topographic impact of subglacial water beneath Mars’ south polar ice cap”

Authors: N.S. Arnold, F.E.G. Butcher, S.J. Conway, C. Gallagher and M.R. Balme

### *Additional Model Data and Results*

Additional input details and results for some model runs are shown in Supplementary Figures 1-2. Initial conditions for the transient runs (see Methods) are shown in Supplementary Figure 1. There is  $\sim 200$  m of relief in the bed topography (Supplementary Fig. 1a) over the area containing the water bodies, which (with the surface elevation (Fig. 1b)), leads to around  $\sim 200$  m of ice thickness variation (Supplementary Fig. 1b). The effect of the LAPS in the NW corner is clearly seen in the thickness distribution; the bed topography here is fairly flat. The calculated steady-state flow velocity (Supplementary Fig. 1c) over the central area shows little spatial variation, with a mean annual velocity of  $\sim 2 \times 10^{-7} \text{ myr}^{-1}$ . The steep slopes over the LAPS lead to the largest velocities in the model domain, around  $10^{-4} \text{ myr}^{-1}$ . The calculated steady-state basal temperature largely reflects the ice thickness distribution. Over the central area (red box in Fig. 1b), basal temperatures vary by  $\sim 2\text{K}$ , with a mean value around 178K. This is very similar to the value calculated by Sori and Bramson<sup>9</sup>. The effect of the thinner ice beneath the LAPS is clearly seen, with basal temperatures of around 175K. The flow-induced elevation changes (Supplementary Fig. 1e) are very small over the central area, around  $10^{-5}$  m over the 1000 year run duration, although they reach  $\sim \pm 0.2$  m in the area at the crests of the LAPS due to the steep slopes and much faster resulting ice flow in this area. These values result in an annual synthesised mass balance of  $\sim 10^{-8} \text{ myr}^{-1}$  in the central part of the model domain (Supplementary Fig. 1f).

Supplementary Figure 2 shows additional results for Runs M1 and S9 (shown in Fig. 2a and b). The modelled ice velocity after 500 kyr (Supplementary Fig. 2a, Run M1) and 1 Myr (Supplementary Fig. 2b, Run S9) shows the enhancement due to sliding and softening of the ice due to geothermal heating. Velocity over the water bodies increases by a factor of  $\sim 600$  (compared with the steady state velocity, Supplementary Fig. 1c) for Run M1, and by a factor of  $\sim 50$  for Run S9. Thermally-driven softening increases the velocity over a larger area than sliding, but generally by a lower amount; by factors of  $\sim 100$  and  $\sim 10$  for Runs M1 and S9 respectively. Calculated basal temperatures for Runs M1 and S9

are shown in Supplementary Figs. 2c and d. For  $90\text{mWm}^{-2}$  (Run M1, Supplementary Fig. 2c), the basal temperature over the heated area increases to a mean of around 217K. This is approximately 15K higher than the values calculated by Sori and Bramson<sup>9</sup>. This could be partly due to the simpler conductivity structure used in this study with uniform conductivity within the SPLD, although the steady state temperature (Supplementary Fig. 1c) suggests this is not an important effect. Instead, the higher calculated temperatures with high excess geothermal heat result from the strain heating feedback generated by the enhanced ice flow which forms an important additional source of basal heating, as argued by Butcher et al.<sup>10</sup> The calculated mean basal temperature for a geothermal heat flux of  $60\text{mWm}^{-2}$  (Run S9, Supplementary Fig. 2d) is around 198K over the heated area. This is only slightly lower than the value for  $72\text{mWm}^{-2}$  from Sori and Bramson<sup>9</sup>, again showing the important additional heating component due to strain heating from enhanced flow.

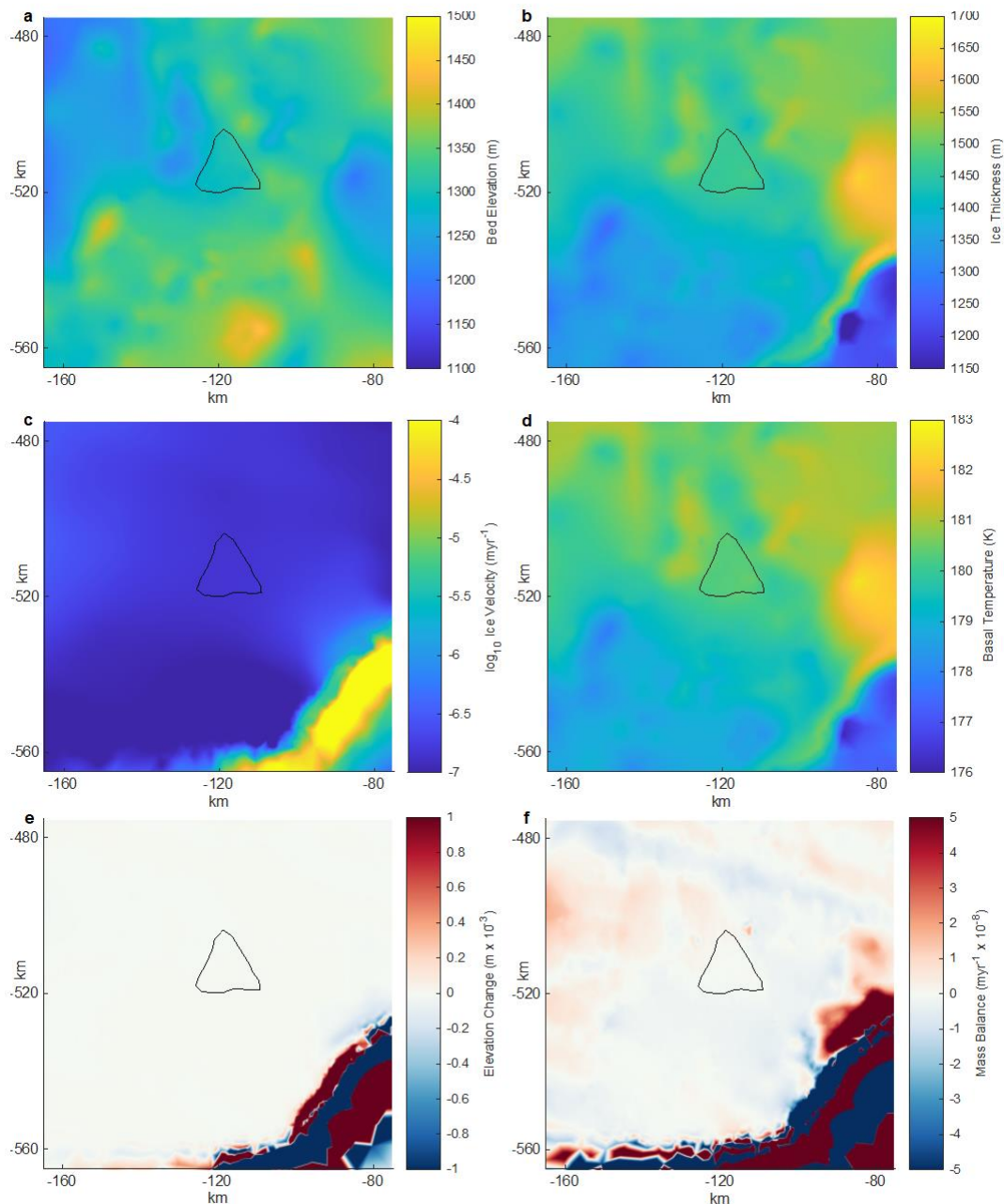
Runs C11 - C14 (not shown) show that decreasing (increasing) ice thermal conductivity raises (lowers) the modelled basal temperature by a few K, leading to a slight enhancement (reduction) in elevation changes, mimicking a small increase (decrease) in excess geothermal heating. Altering ice density (to that of pure ice) has a similar effect to higher thermal conductivity via a different mechanism; it reduces calculated gravitational driving stress, lowering ice velocity and slightly reducing strain-induced heating, mimicking a slightly smaller level of excess geothermal heat. Acting together, lower ice conductivity has a slightly larger effect.

Run NS5 (not shown), with no sliding permitted but elevated GHF of  $72\text{mWm}^{-2}$ , shows a  $\sim \pm 0.25\text{m}$  elevation height change in 500 kyr, with the largest values at the edge of the heated area, (as can be seen in Fig. 2a). The height change is less than that observed for run S9, showing that allowing basal sliding leads to more rapid and larger elevation changes than geothermal heating alone. Run NS10 (not shown) showed no long-term evolution of the surface topography due to possible effects of the basal topography on ice flow alone after a 10 My integration.

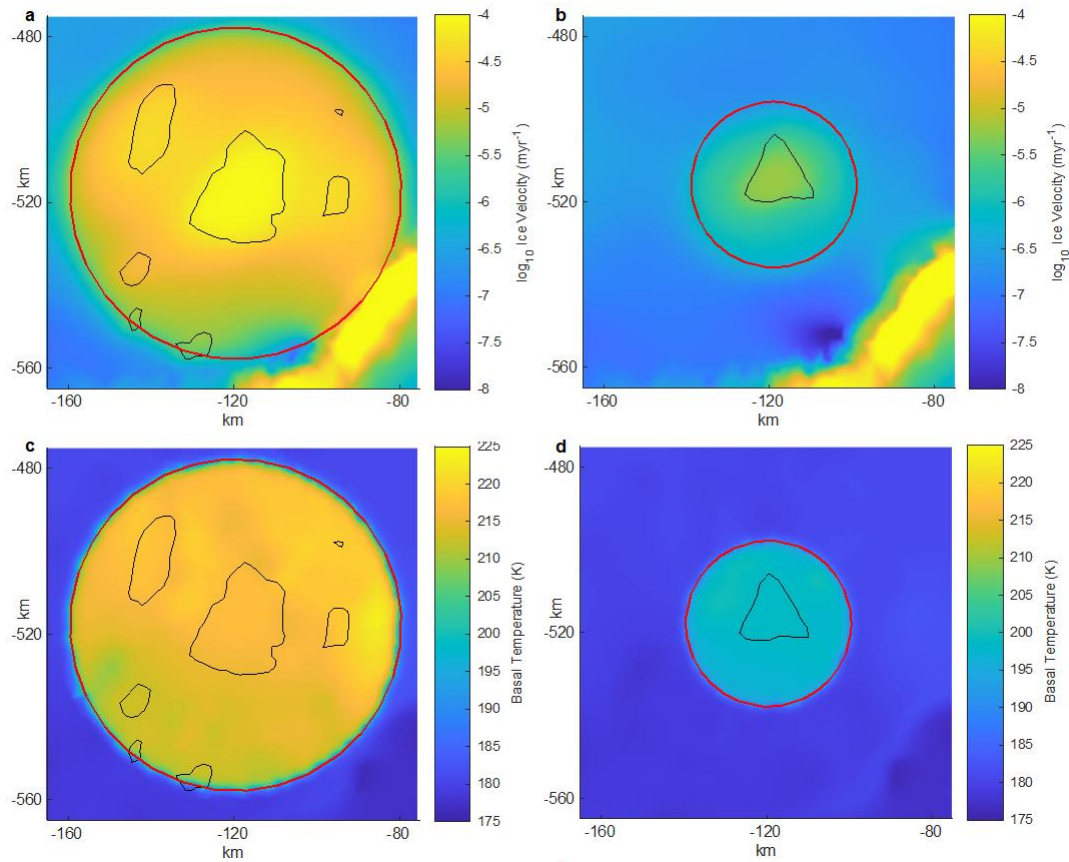
We also performed a set of runs (not shown) where the final conditions of Run S9 formed the initial conditions, and in which the geothermal anomaly was removed and sliding was prevented (simulating the end of the possible geothermal event, and re-freezing of the bed). The re-freezing results in a very rapid decrease in basal velocity over the

immediate area that was previously allowed to slide. The geothermally-induced increase in basal temperature diffuses away rapidly, at an exponentially-decreasing rate. After 500 kyr, the basal temperature in the heated areas is  $\sim 2$  K above the initial value (shown in Supplementary Fig. 1d), and is within 0.5 K of the initial temperature by 2.5 Myr. The elevation changes due to heating and sliding result in a very small change in driving stress such that the elevation changes decay, but extremely slowly due to the very slow modelled ice velocity. After 10 Myr, the elevation anomalies have been reduced by  $\sim \pm 5 \times 10^{-3}$  m.

## Supplementary Figures



**Supplementary Figure 1. Boundary and initial conditions for the central area of the model domain (red square in Fig. 1b) for transient model runs. a.** MARSIS bed elevation<sup>27</sup>. **b.** MARSIS-derived SPLD thickness. **c.** Modelled steady state ice velocity (note logarithmic scale). **d.** Steady-state basal temperature. **e.** Modelled surface elevation change after 1000 model years without sliding or excess geothermal heating. **f.** Assumed surface mass balance from e. Outlines and axes as Fig. 1.



**Supplementary Figure 2. Additional model results for runs M1 and S9 for the central area of the model domain (red box in Fig. 1b) for transient model runs. a.** Modelled ice velocity for run M1 after 500 kyr. **b.** Modelled ice velocity for run S9 after 1 Myr. **c.** Modelled basal temperature for Run M1 after 500kyr. **d.** Modelled basal temperature for Run S9 after 1 Myr. Outlines and axes as Fig. 2.

## Supplementary Tables

Run	Elevated GHF (mWm <sup>-2</sup> )	Radius of heating (km)	Sliding allowed	Parameters (Std denotes as Table S1)
M1	90	40	M	Std
M2	72	40	M	Std
M3	60	40	M	Std
M4	90	30	M	Std
M5	72	30	M	Std
M6	60	30	M	Std
M7	90	20	M	Std
M8	72	20	M	Std
M9	60	20	M	Std
M10	30*	-	M	Std
S1-S10	As M1-10	As M1-10	S	Std
C1-C10	As M1-10	As M1-10	C	Std
L1-L10	As M1-10	As M1-10	L	Std
LL6	As M6	30**	L	Std
C11	60	30	C	$\rho = 917 \text{ kgm}^{-3}$
C12	60	30	C	$k = 2.0 \text{ Wm}^{-1}\text{K}^{-1}$
C13	60	30	C	$k = 3.0 \text{ Wm}^{-1}\text{K}^{-1}$
C14	60	30	C	$\rho = 917 \text{ kgm}^{-3}, k = 2.0 \text{ Wm}^{-1}\text{K}^{-1}$
NS5	72	30	No sliding	Std
NS10	30*	-	No sliding	Std

**Supplementary Table 1. Model Runs.** M denotes sliding allowed over the multiple water bodies<sup>2</sup>. S denotes over the single central water body<sup>1</sup>. C denotes sliding over a circular water body in the location of the single water body of radius 12 km. L denotes over a lozenge-shaped area derived from the topographic bench identified here. 30\*\* denotes an enlarged lozenge-shaped area equivalent to a 30km radius circle. \* denotes nominal background geothermal heat for model domain<sup>9</sup>.

Parameter	Value	Source
SPLD Surface Temperature	162 K	9
Background Geothermal Heat Flux	30 mWm <sup>-2</sup>	9
Ice Density ( $\rho$ )	1100 kgm <sup>-3</sup>	2
Ice Thermal Conductivity (k)	2.4 Wm <sup>-1</sup> K <sup>-1</sup>	29
$G$ (Gravitational acceleration)	3.711 ms <sup>-2</sup>	-

**Supplementary Table 2. Standard Model Parameters**